NASICON-type Medium Entropy $Li_{1.5}Sn_{1.0}Al_{0.5}Zr_{0.5}(PO_4)_3$ Electrolyte for Solid State Li Metal Batteries

Pratiksha Gami[a], Manish Badole[a], Hari Narayanan Vasavan[a], Asish Kumar Das[a], Samriddhi Saxena[a], Neha Dagar[a], Velaga Srihari[c], and Sunil Kumar[a,b]*

[a]Department of Metallurgical Engineering and Materials Science, Indian Institute of Technology Indore, Simrol, 453552, India.

[b]Center for Electric Vehicle and Intelligent Transport Systems, Indian Institute of Technology Indore, Simrol, 453552, India

[c]High Pressure & Synchrotron Radiation Physics Division, Bhabha Atomic Research Centre, 400085 Mumbai, India

* Corresponding author

Corresponding author E-mail: sunil@iiti.ac.in

Abstract

Developing solid electrolytes for all-solid-state lithium batteries with superior performance is crucial for portable energy storage. This study uses a traditional solid-state reaction technique to fabricate a NASICON-type medium entropy $Li_{1.5}Sn_{1.0}Al_{0.5}Zr_{0.5}(PO_4)_3$ (LSAZP) ceramic electrolyte. The Rietveld refinement of room temperature X-ray diffraction (XRD) data confirms a pure rhombohedral phase ($R\bar{3}c$) for LSZAP ceramic sintered at 1050 °C. Temperature-dependent synchrotron XRD data demonstrates an increase in lattice parameter *c* with a positive coefficient of thermal expansion ($+2.40 \times 10^{-5}$ K^{-1}) and a negative coefficient of thermal expansion (-1.26×10^{-6} K^{-1}) for the lattice parameter *a* with increasing temperature. Interestingly, despite the anisotropic thermal expansion, no intergranular cracks, typically observed in rhombohedral NASICON-type phases, are noticeable in the scanning electron micrographs of the LSAZP samples. The sample sintered at 1050 °C (relative density ~ 90%) exhibits an excellent room temperature conductivity of ~ 2.95×10^{-4} S cm^{-1} and activation energy ~ 0.39 ± 0.02 eV. The Li-ion transference number is ~ 0.99, suggesting that Li-ion is the dominant charge carrier in the sample. During galvanostatic lithium plating-stripping tests, the symmetric Li|LSAZP|Li cell demonstrates excellent lithium plating-stripping stability over 50 h at a current density of 4 µA cm^{-2}.

Keywords

Solid-state electrolyte; NASICON; Medium entropy oxide; Ionic conductivity;

Electrochemical performance

1. Introduction

Rechargeable batteries have the potential to revolutionize clean energy storage systems and are ubiquitously employed in portable electronics and electric vehicles [1-3]. Li-ion batteries are an important electrochemical energy storage technology in the market and are useful in many applications [4-7]. The conventional Li-ion battery uses flammable organic electrolytes that allow alkali-ions to transport between electrodes. Employing organic liquid electrolytes typically raises serious safety issues. It could cause a fire and lead to explosions in the event of a thermal runaway or an electrolyte leakage from a malfunctioning battery [8-13]. Furthermore, as this family of organic electrolytes is typically incompatible with Li metal electrodes (due to lithium dendrite growth during prolonged cycling), it tends to be used with graphite anodes [11, 14-16]. Utilizing Li metal as an anode has benefits, like high specific capacity (i.e., ~ 3680 mAh/g) and lowest reduction potential (i.e., -3.04 V vs. SHE) [14, 17]. A workable solution to the problem of using organic liquid electrolytes is to use solid-state electrolytes (SSEs), which have a larger operating temperature range, lower flammability, negligible electron conductivity, volatility, and lower toxicity [18-26]. There are numerous reports of Li-ion conducting solid electrolytes throughout the past 50 years dealing with NASICON-type, garnet-type, sulfide-type, perovskites, amorphous oxides, polymers, etc., which are promising candidates to be employed in solid-state batteries as an electrolyte [27-32].

As most Li^+ conducting solid electrolytes are sensitive to moisture, handling them in an open environment can be challenging, particularly for the high conductivity thio-LISICON-typed solid electrolytes [33]. NASICON-type lithium-ion conducting electrolytes are attractive solid-state materials among the other candidates as these are reasonably moisture stable and can be processed in an open-air environment. These materials typically crystallize in a rhombohedral lattice

composed of phosphate tetrahedra sharing corners with MO_6 octahedra, creating three-dimensional (3D) channels for the Li^+ transport [25, 34-36]. Various NASICON-type crystal structures are being investigated with the general formula $LiM_2(PO_4)_3$, in which M can be any tetra-valent atom from the p/d/f-block of the periodic table. Examples of NASICON-type ceramic electrolytes include $LiTi_2(PO_4)_3$ (LTP), $LiZr_2(PO_4)_3$ (LZP), $LiGe_2(PO_4)_3$ (LGP), $LiSn_2(PO_4)_3$ (LSP), etc., and other compositions based on these materials with various dopants [37-40]. It has been demonstrated that partially substituting certain aliovalent elements for M can boost the Li-ion conductivity by raising the concentration of Li-ions in the formula unit (i.e., demonstrating the effectiveness of doping in introducing extra Li-ions at the interstitial sites) and expanding the bottleneck area for Li^+ to move. The lithium-ion conductivity of the Al-doped LTP and LGP materials is high (> 10^{-4} S/cm), but Ti^{4+} gets reduced when LTP is in touch with the metallic lithium, and Ge in LGP is quite expensive [30]. On the other hand, LZP shows superior electrochemical stability towards the Li anode because the energy of the zirconium/zirconium-ion redox pair exceeds the entropy level of the Li metal [30, 31, 39, 41-44]. Similarly, LSP can be synthesized at temperatures as low as 900 °C in a single-phase triclinic structure (space group: $P\bar{1}$) [45]. However, fast Li-ion conducting rhombohedral LSP, which requires higher calcination temperatures, is accompanied by SnO_2 as the impurity phase [38].

Recently, there have been reports where multi-cations at M-site stabilized the rhombohedral phase at lower calcination temperatures and enhanced the Li-ion migration [46-48]. The high-entropy materials (more than 5 different cations at M-site) with the NASICON framework have also gained attention as these exhibited superior electrical and electrochemical behavior [49-51]. In this study, a medium entropy (S_{config} = 1.04R) $Li_{1.5}Sn_{1.0}Al_{0.5}Zr_{0.5}(PO_4)_3$ sample was prepared *via* solid-state method at different sintering temperatures [52]. The effects of sintering temperature on the

densification and electrical properties were investigated using various techniques such as X-ray diffraction (XRD), field-emission scanning electron microscope (FESEM), and impedance spectroscopy. The $Li_{1.5}Sn_{1.0}Al_{0.5}Zr_{0.5}(PO_4)_3$ ceramic sintered at 1050 °C exhibited an exceptional total conductivity of 2.95×10^{-4} S cm^{-1} at room temperature (Table S1).

2. Materials and Methods

A solid-state reaction method was adopted to fabricate the polycrystalline $Li_{1.5}Sn_{1.0}Al_{0.5}Zr_{0.5}(PO_4)_3$ (LSAZP) ceramic samples. Corresponding stoichiometric amounts of lithium carbonate (Li_2CO_3), zirconium oxychloride ($ZrOCl_2 \cdot 9H_2O$), alumina (Al_2O_3), ammonium dihydrogen phosphate ($NH_4H_2PO_4$) and tin (IV) oxide (SnO_2) were mixed using agate and mortar, followed by a planetary ball mill in EtOH for 12 h at 300 rpm. An excess of 10% Li_2CO_3 was used to offset the loss of lithium. The ceramic slurry was dried at 80 °C for 12 h to eliminate EtOH. The dried powder was heated for 12 h at 600 °C in a box furnace. The powder was then ground for 6 h in a planetary ball mill and was allowed to dry overnight. The resulting powder was then uniaxially compressed under 150 MPa to fabricate disc-shaped pellets (~10 mm diameter). All the green ceramic pellets were heated at different temperatures to determine the optimal temperature for sintering. A sacrificial powder of the same stoichiometry was used to cover all the ceramic discs to minimize lithium loss during reactive sintering at temperatures higher than 950 °C.

X-ray diffraction (XRD) patterns for the prepared ceramics were acquired using an Empyrean - Malvern Panalytical diffractometer with monochromatic Cu-kα radiation (2θ range: 10°–60°). To assess the lattice parameters and sample density, the TOPAS Academic (version 6) software was used for the Rietveld refinement of the XRD data [53]. The selected LSAZP sample was maintained at various temperatures in the 50–550 °C range during the heating-cooling cycle for the temperature-dependent XRD measurements. The extreme condition angle dispersive/energy

dispersive X-ray diffraction (EC-AD/ED-XRD) Beam Line (BL-11) at Indus-2 synchrotron source, Raja Ramanna Centre for Advanced Technology, Indore (India), was used for this experiment. The wavelength of λ = 0.7301(4) Å X-ray beam was used. The microstructures and elemental compositions of as-prepared ceramic pellets were obtained by a FESEM (model: JEOL-7610+) equipped with an energy-dispersive X-ray spectrometer (EDS). An LCR meter (Make: NF Corp., ZM2376) was used to measure the electrical conductivity of the as-sintered pellets in the frequency range of 1 Hz to 1 MHz. The ceramic pellets were dried at 120 °C to remove additional moisture before the impedance measurements. All the ceramic discs were coated with silver paste on the flat sides. The impedance data were fitted using a suitable equivalent circuit model with the software EIS analyzer [54]. Using the Keithley Source Meter Unit (model 2450-EC), the electronic conductivity and lithium-ion migration number were determined through chronoamperometry by applying a DC polarization of 1 V across the sample. A lithium plating/stripping cycle test was conducted at varying areal current densities on symmetric Li|LSAZP|Li cells in a Swagelok-type cell.

3. Results and Discussion

Room temperature powder X-ray diffraction was carried out to ascertain the phase formation at different sintering temperatures. Figure 1(a) depicts the XRD patterns of LSAZP-T (where T denotes the sintering temperature: 900, 950, 1000, 1050, and 1100 °C) samples sintered for 12 h at various temperatures (900 °C to 1100 °C). At T = 900 and 950 °C, samples have triclinic ($P\bar{1}$) and rhombohedral ($R\bar{3}c$) mixed phases. With the increase in the sintering temperatures, the phase fraction of the rhombohedral phase increases, and peaks corresponding to the triclinic phase disappear in the patterns for the samples sintered at 1050 °C (denoted as LSAZP-1050). Additional minor impurity phases of aluminum phosphate and tin (IV) oxide appeared in the samples sintered

above 900 °C. The rhombohedral unit cell volume increased with an increase in sintering temperature. The unit cell volume and lattice constants for all samples calculated using the TOPAS Academic (version 6) software are displayed in Table 1. The rhombohedral unit cell volume increases with the increases in sintering temperature, which could be attributed to the better crystallization and larger average grain size in samples sintered at higher temperatures.

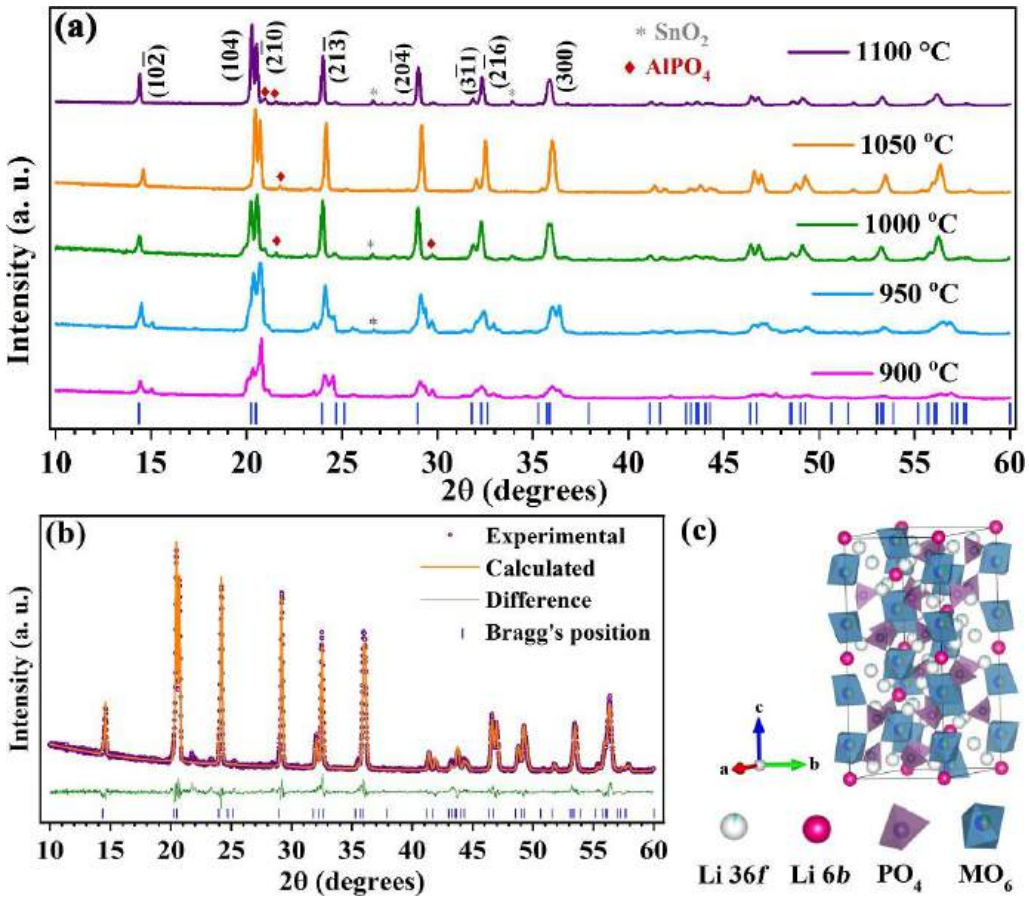

Fig. 1. (a) Room temperature powder XRD patterns of LSAZP samples sintered at different temperatures, (b) X-ray diffraction Rietveld refinement pattern of $Li_{1.5}Sn_{1.0}Al_{0.5}Zr_{0.5}(PO_4)_3$ *sample prepared at 1050 °C. The violet open circles represent experimental data, the orange line is for the calculated pattern, the olive line shows the difference curve, and (c) the crystal*

structure for LSAZP. The vertical bar markers (blue) at the bottoms of (a) and (b) are for diffraction peak positions expected from the rhombohedral R3̄c phase.

Table 1: Crystallographic data of LSAZP samples sintered at different temperatures obtained from the Rietveld refinement of room temperature XRD data.

Sinntering Temperature (°C)	**Lattice parameter (Å)**	**α, β, γ (°)**	**Volume (Å^3)**	**Space group**
900	*a* = 8.406(5) *b* = 8.451(4) *c* = 8.874(4)	118.31(3), 89.85(3), 119.59(3)	460.07(6)	*P*1̄
	a = *b* = 8.570(2) *c* = 21.669(7)	90, 90,120	1378.5(8)	*R*3̄*c*
950	*a* = 8.422(4) *b* = 8.448(3) *c* = 8.899(3)	118.26(3),89.42(3), 120.13(3)	460.32(5)	*P*1̄
	a = *b* = 8.600(1) *c* = 21.688(5)	90, 90,120	1387.4(6)	*R*3̄*c*
1000	*a* = *b* = 8.636(4) c = 21.6428(1)	90, 90,120	1398.10(1)	*R*3̄*c*
1050	*a* = *b* = 8.664(4) *c* = 21.616(1)	90, 90,120	1405.18(1)	*R*3̄*c*

1100	$a = b = 8.6640(4)$ $c = 21.6136(1)$	90, 90,120	1410.3(4)	$R\bar{3}c$

Figure 1(b) displays the experimental and fitted XRD patterns of the LSAZP-1050 pellet, which validates the rhombohedral structure of the prepared ceramic. The solid, orange-colored line represents the Rietveld refined profile, whereas the violet-colored open circle symbols represent the observed XRD data. The olive line indicates the difference curve, while the blue vertical bars reflect the computed Bragg's peak positions for the space group $R\bar{3}c$. A 6-order polynomial function was utilized to refine the background, and the pseudo-Voigt II function was employed to model the peak profile with an asymmetry correction based on sample displacement error and axial divergence. The refined atomic coordinates, occupancy, and Wyckoff positions in the LSAZP-1050 framework are given in Table 2. The lattice parameters of the LSAZP-1050 rhombohedral phase were calculated to be $a = b = 8.664(4)$ Å and $c = 21.616(1)$ Å, with a unit cell volume of 1410.18(14) Å^3 (for $LiZr_2(PO_4)_3$, $a = b = 8.8532(6)$ Å, $c = 22.2531(4)$ Å and $V = 1510.18(1)$ Å^3; for $LiSn_2(PO_4)_3$, $a = b = 8.6285(2)$ Å, $c = 21.5258(7)$ Å and $V = 1388.56(9)$ Å^3) [38, 39]. It is to be noted that the effective ionic radius of the M-site for LSAZP is ~ 0.659 Å (ionic radii for octahedrally coordinated Zr^{4+} = 0.72 Å, Sn^{4+} = 0.69 Å, and Al^{3+} = 0.535 Å); accordingly, the volume of LSAZP unit cell is expected to be smaller than that of both LZP and LSP [55]. The observed higher unit cell volume for the LSAZP sample compared to the LSP is attributed to the additional 0.5 Li-ions per formula unit cell.

Table 2: Various crystallographic parameters of LSAZP-1050 obtained from the Rietveld refinement of room temperature powder XRD data. (R_{wp}(%) = 10.23; R_p(%) = 5.22 and GOF = 1.96)

Site	Wyckoff position	*x*	*y*	*z*	Atom	Occupancy
Li1	6*b*	0	0	0	Li^{+1}	1
Li2	36*f*	0	0.25	0.05	Li^{+1}	0.0833
Zr	12*c*	0	0	0.14(3)	Zr^{+4}	0.25
Al	12*c*	0	0	0.14(3)	Al^{+3}	0.25
Sn	12*c*	0	0	0.14(3)	Sn^{+4}	0.50
P	18*e*	0.29(4)	0	0.25	P^{+5}	1
O1	36*f*	0.17(6)	0.98(8)	0.19(2)	O^{-2}	1
O2	36*f*	0.19(4)	0.17(6)	0.08(3)	O^{-2}	1

The crystal structure of rhombohedral LSAZP generated using the crystallographic data obtained through Rietveld refinement is shown in Fig. 1(c). The formula unit cell consists of phosphate tetrahedra (PO_4) and MO_6 octahedra. Each tetrahedral unit shares oxygen with four octahedra. The phosphate and MO_6 polyhedra are alternated in a rhombohedral NASICON framework, creating 3D tunnels for better Li^+ mobility. As a result, modifications to these factors may impact how well Li-ions move in these materials. As shown in Fig. 1(c), there are two distinct types of Li-ion sites (Li1-6*b*, Li2-36*f*) in which the 6*b* sites are fully occupied. Chen and Adams's softBV software was used to obtain the Li-ion migration route over the LSAZP-1050 crystal structure using the CIF obtained from the Rietveld refinement of the XRD data. Figure S1 displays the results of the BVPA algorithm plotted using the VESTA software [56]. This image represents the 3D-linked Li-ion migration pathways in LSAZP-1050.

Synchrotron powder XRD was performed to gain a better understanding of how the temperature affects the thermal expansion of the rhombohedral unit cell on the LSAZP-1050 sample. Figure 2(a) displays the XRD patterns at various temperatures in the 50 to 550 °C range during heating and cooling, and the enlarged view of 2θ from 9.39° to 9.78° is shown in Fig. 2(b).

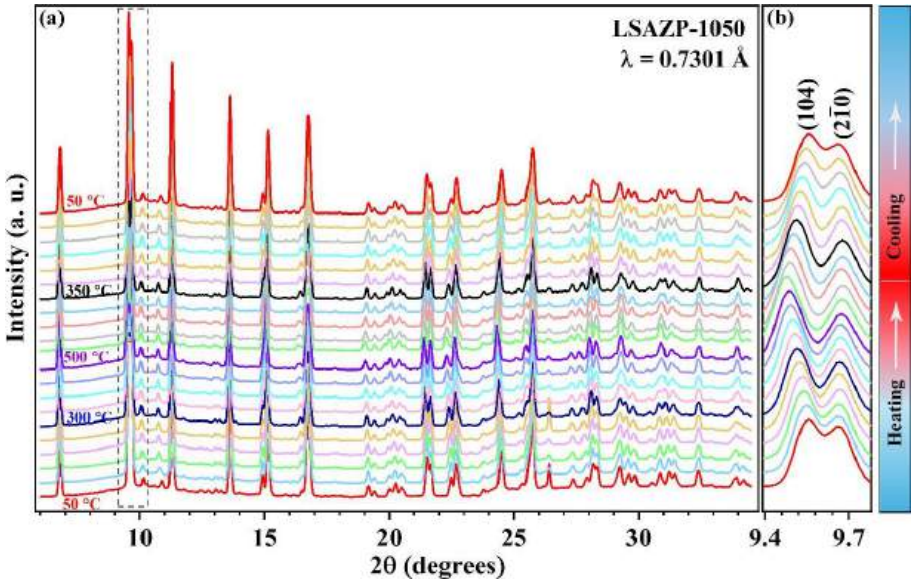

Fig. 2. (a) Temperature-dependent synchrotron XRD patterns of LSAZP-1050 sample and (b) Magnified view of 2θ in 9.39° to 9.78° region of (a).

With the increasing temperature, the (104) peak position shifts towards the lower 2θ, the splitting between (104) and $(2\bar{1}0)$ peaks increase, and these trends reverse upon decreasing the temperature back to 50 °C. The shift in the (104) peak position indicates the increase in the interplanar spacing $d_{(104)}$ during heating. To further quantify the changes in the lattice parameters *a* and *c*, Le Bail fitting of the temperature-dependent SXRD data was performed using the software TOPAS Academic. The variation of the *a* and *c* with temperature during heating is shown in Fig. 3. The lattice parameter *a* shows a small decrease with increasing temperature, whereas the lattice parameter *c* increases linearly. The coefficients of thermal expansion for *a* and *c*, in the temperature range of 50 °C to 550 °C, are -1.26×10^{-6} K^{-1} and $+2.40 \times 10^{-5}$ K^{-1}, respectively. Such anisotropic

thermal expansion of the rhombohedral unit cell in NASICON-type ceramics is known to cause cracks and resultant anti-sintering behavior, leading to poor densification [38, 57-59].

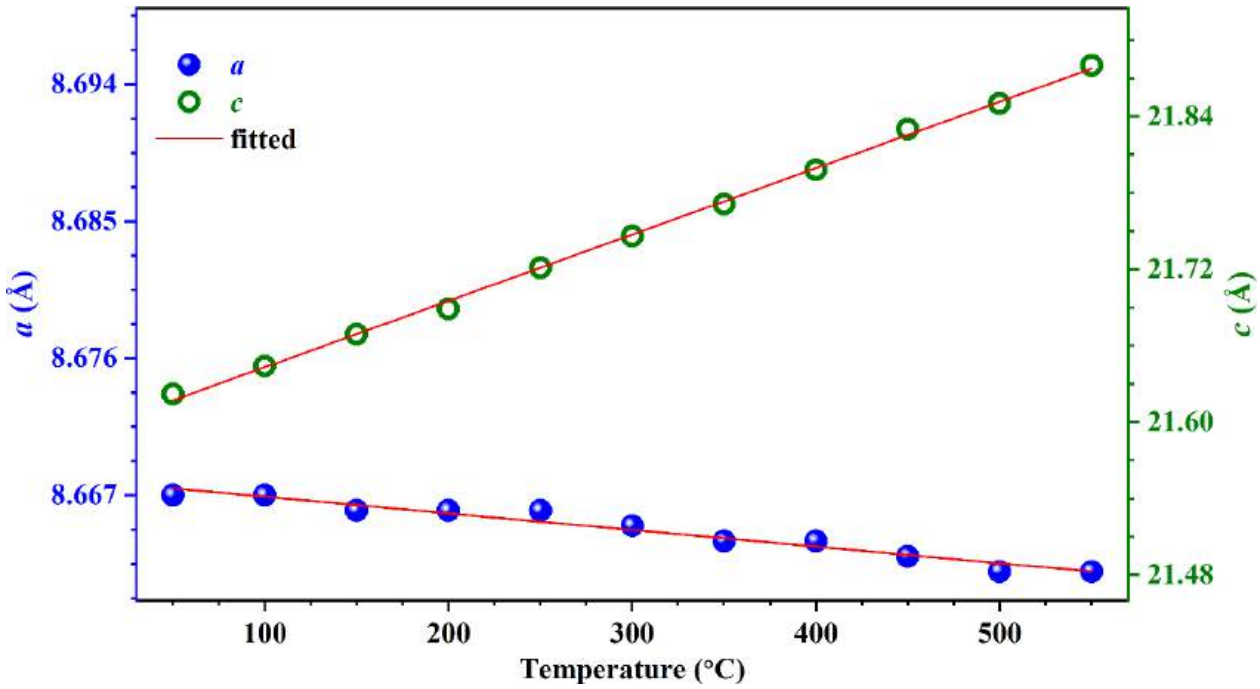

Fig. 3. Variation of lattice parameters (a & c) with temperature for LSAZP-1050 sample.

The morphology of the as-sintered ceramic pellets was investigated (Fig. 4, Figs. S2 - S5) *via* FESEM. The LSAZP-900 sample exhibited smaller grains with an average grain size of ~ 1.2 µm. With the increase in the sintering temperature, the average grain size of the samples progressively increases from ~ 1.2 µm for LSAZP-900 to ~2.7 µm for LSAZP-1100. Interestingly, micrographs also revealed no microcracks in LSAZP pellets. Inter- & intra-granular microcracks, and those along the grain boundaries, are known to cause poor densification in NASICON-type solid electrolytes, and it is suggested that a grain size of less than ~ 4 µm is required to prevent significant microcracking [60]. The absence of microcracks can be attributed to the observed smaller grains in LSAZP pellets. EDS elemental mapping was used to determine the elemental distributions in all as-prepared samples, and the resulting images are displayed in Fig. 4 and Figs. S2 - S5. These figures show a uniform distribution of Zr, Al, Sn, P, and O elements throughout the samples, and

elemental segregation is apparent in any samples. The relative density of LSAZP pellets sintered at different temperatures is given in Table S2. A low relative density of 79% was observed for the ceramic sample sintered at 900 °C. The relative density value increased with an increase in temperature, and the highest relative density of 90% was achieved for the sample sintered at 1050 °C. Upon increasing the sintering temperature further to 1100 °C, the relative density decreased again to ~ 87%, which may have been caused by the volatilization of Li at higher sintering temperatures (Table S2).

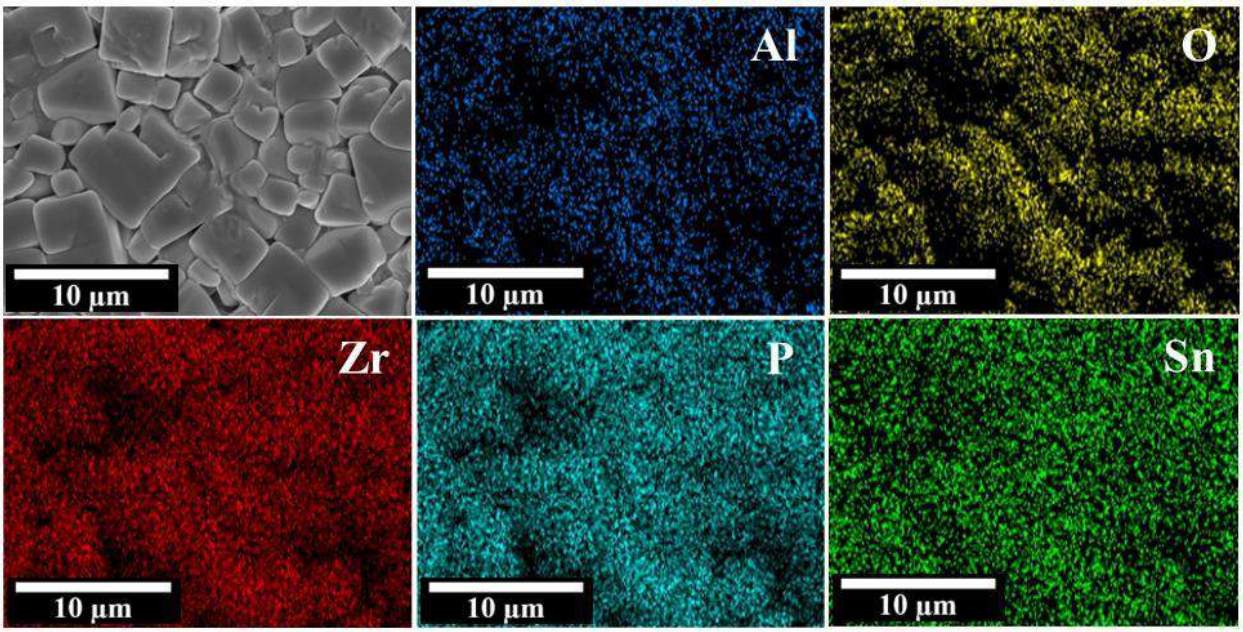

Fig. 4. SEM micrograph and EDS mappings of various elements of LSAZP pellet sintered at 1050 °C.

In order to evaluate the impact of sintering temperature on ionic conductivity, silver paint was coated evenly across the flat sides of dense LSAZP electrolyte pellets, and the impedance data was measured over the 1 Hz to 1 MHz frequency range [61]. The room temperature impedance data for different ceramic samples in Nyquist plots are shown in Fig. 5. The total resistance was calculated by fitting impedance data using an equivalent circuit consisting of a constant phase element (CPE_{elect}) connected in series with a parallel combination of resistance R1 & CPE1. Here,

R1 represents the total resistance, and CPE_{elect} reflects the contribution from the ion-blocking Ag electrodes [10, 62]. At high frequencies, all samples show a single semi-circular arc depicting the bulk and grain boundary (GB) resistances. The occurrence of ion-blocking electrode polarization is responsible for the straight line seen in the low-frequency region of the graphs.

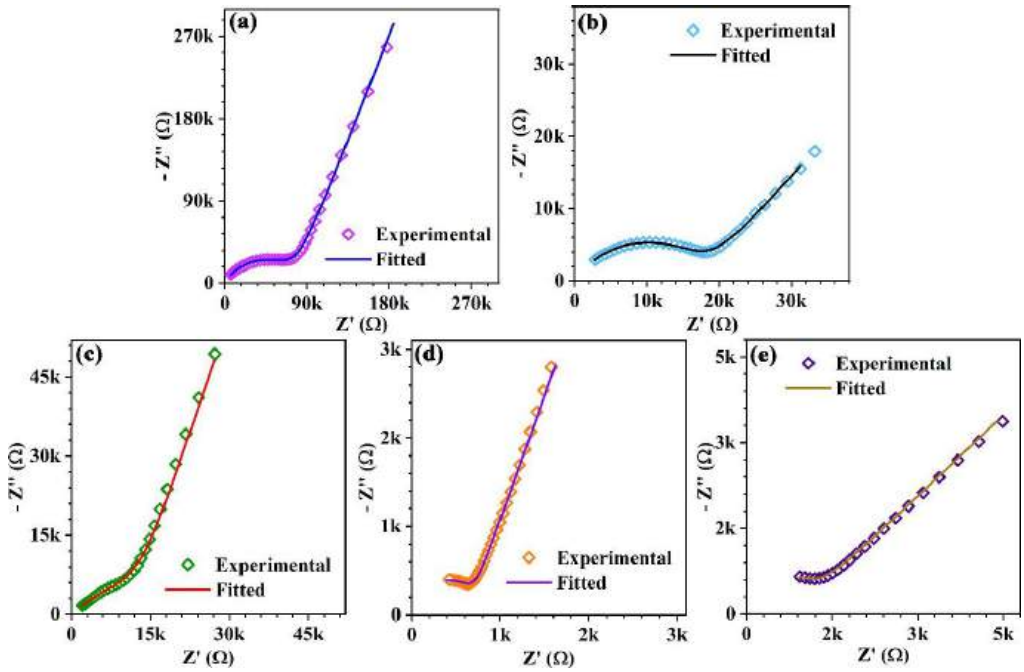

Fig. 5. RT Nyquist plots in 1 MHz to 1 Hz frequency range of LSAZP pellets sintered at different temperatures: (a) 900 °C, (b) 950 °C, (c) 1000 °C, (d) 1050 °C and (e) 1100 °C. The solid line passing in plots is the fitted impedance data using an (R1||CPE1) + (CPE_{elect}) equivalent circuit.

The conductivity values were calculated using the fitted values of R1 and the pellets' dimensions. As can be seen from Table 3, the value of room temperature conductivity increases from ~ 4.70 × 10^{-6} S cm^{-1} for the LSAZP-900 sample to the highest value of ~ 2.47 × 10^{-4} S cm^{-1} for the sample calcined at 1050 °C. This result could be explained by better densification, larger average grain size, and increased unit cell volume with sintering temperature. Further increase in the sintering temperature decreased the total conductivity to ~ 8.82 × 10^{-5} S cm^{-1} for LSAZP-1100. This

decrease in conductivity of the sample sintered at 1100 °C could be attributed to the increased lithium volatilization. High-temperature treatment can lead to lithium volatilization, resulting in the formation of impurity phases (e.g., $AlPO_4$, SnO_2). SnO_2 and $AlPO_4$ act as Li^+ insulating phases, obstructing lithium-ion transport at grain boundaries and thereby impairing the overall conductivity [63].

Table 3: Conductivity of LSAZP pellets sintered at different temperatures. σ^m and σ^0 represent the measured total conductivity and the conductivity after the porosity correction, respectively.

Sintering Temperature (°C)	**σ^m (S cm^{-1})**	**σ^0 (S cm^{-1})**
900	4.70×10^{-6}	6.86×10^{-6}
950	1.01×10^{-5}	1.32×10^{-5}
1000	2.75×10^{-5}	3.42×10^{-5}
1050	2.47×10^{-4}	2.95×10^{-4}
1100	8.82×10^{-5}	1.09×10^{-4}

LSAZP pellets sintered at different temperatures have different porosity levels, so the measured conductivity values may not reflect the actual conductivity values. To correct these values for the porosity effect, an EMT (effective medium theory) was employed [64, 65]. In this study, we have used the Bruggeman approximation model to determine the conductivity of the ceramic-air composites using the equation [65, 66]:

$$(1-p)\frac{\sigma^0-\sigma^m}{\sigma^0+2\sigma^m} + p\,\frac{\sigma^i-\sigma^m}{\sigma^i+2\sigma^m} = 0 \quad (1)$$

Where, σ^i is the conductivity of the dispersed phase (air, in this case, $\sigma^i = 0$), σ^0 is the conductivity of the continuous matrix (LSAZP phase with 0% porosity), σ^m is the measured conductivity (total conductivity calculated from impedance data) and p is the volume fraction of the air. With $\sigma^i = 0$, equation 1 reduces to:

$$\sigma^m = \sigma^0 \left(1 - \frac{3}{2}p\right) \quad (2)$$

The grains and pores in this equation are assumed to be randomly distributed. The porosity-corrected values of the total conductivity (σ^0) of different LSAZP samples are given in Table 3. The corrected conductivity (σ^0) of fully dense LSAZP-900 is increased to ~1.46 times (6.86×10^{-6} S cm^{-1}) from its measured value following the porosity adjustment, whereas, σ^0 is estimated to be ~ 2.95×10^{-4} S cm^{-1} (1.19 times of measured value) for the LSAZP-1050 sample.

The temperature-dependent total conductivity σ(T) of each LSAZP sample is shown in Fig. 6. The σ(T) was fitted using the Arrhenius equation ($\sigma = \sigma_0 \exp(-E_a/k_BT)$; k_B is the Boltzmann constant and σ_0 is the pre-exponential factor) and the calculated activation energies are listed in Table S2.

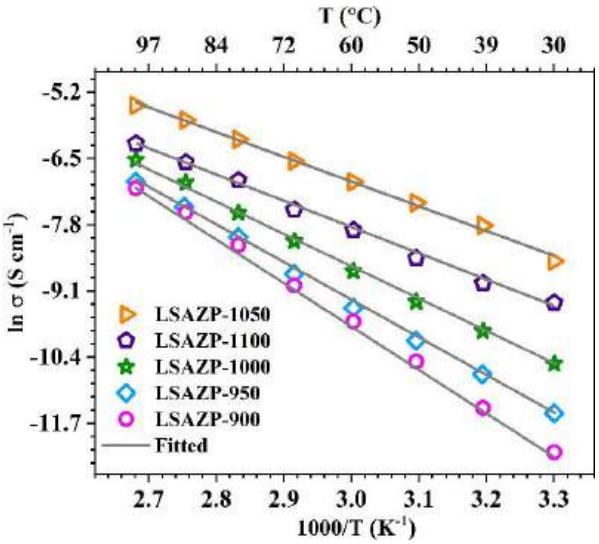

Fig. 6. Arrhenius fitting shows the temperature-dependent total conductivity of the LSAZP samples between 30 to 100 °C.

The lowest value of activation energy (E_a) was estimated to be around 0.39 ± 0.02 eV for the LSAZP-1050. The LSAZP-900 sample exhibited the highest activation energy, ~ 0.76 ± 0.01 eV, which aligns with its lowest conductivity, suggesting a poor lithium-ion migration in this sample. The estimated activation energy value for LZASP-1050 is in the range of those reported for rhombohedral-type NASICON-based fast lithium-ion conductors. The lower activation energy of LSAZP-1050 enables it to have higher ionic conductivity at varying temperatures [39].

A DC polarization study using silver paint as the blocking electrode was conducted in order to evaluate the contribution of lithium-ion conductivity to overall conduction in the LSAZP-1050 sample. Fig. 7(a) illustrates the variation in current over time after a DC polarization of 1 V is applied across the Ag|LSAZP-1050|Ag pellet. As silver electrodes block Li^+, the steady-state current is only due to electronic charge carriers [67, 68]. The Li^+ transference number (t_{Li}^+) was calculated using the relation $t_{Li}^+ = 1 - (I_e/I_t)$, where I_t denotes the initial current, and I_e is the steady-state current. The value of t_{Li}^+ was determined to be ~ 0.99, which puts Li^+ as the dominant conducting species in the LSAZP-1050. The electronic conductivity of all LSAZP samples is shown in Table S3.

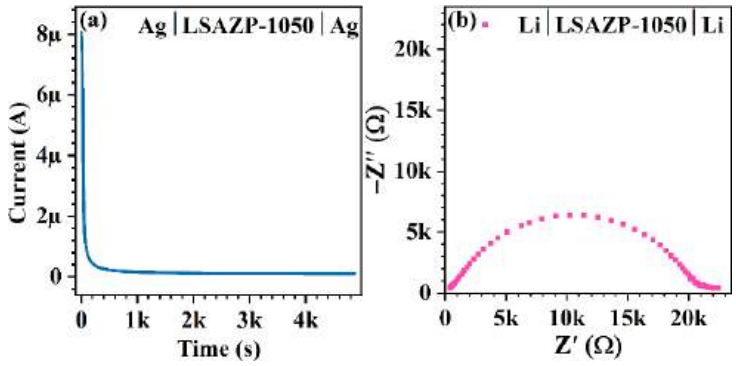

Fig. 7. (a) Chronoamperometry profile of Ag|LSAZP-1050|Ag cell at constant DC polarization voltage of 1 V at RT. (b) RT Nyquist plot of the symmetric Li|LSAZP-1050|Li cell.

The electrochemical compatibility of as-prepared LSAZP and Li metal electrodes was examined using a symmetric Li|LSAZP-1050|Li cell. The impedance data measured at RT on a fresh symmetric cell (Fig. 7(b)) showed a high resistance. This high resistance of ~ 20 kΩ could be attributed to a highly resistive interface between LSAZP and Li. The symmetric Li|LSAZP-1050|Li cells were cycled at various current densities in order to investigate the stability of the Li/LSAZP interface with Li dissolution/deposition (Fig. 8). Fig. 8(b) indicates a highly stable Li/LSAZP interface at low current densities (4 μA cm^{-2}) for more than 50 cycles. Cycling the Li|LSAZP-1050|Li cells at higher current densities (8 μA cm^{-2}) caused the overpotential to increase significantly even under constant current, which makes the solid electrolyte unsuitable for practical applications. This might be due to a high resistive Li/LSAZP interface arising from an inadequate solid-solid contact between the ceramic sample and the lithium metal or a high Schottky barrier of the Li/LSAZP interface [69].

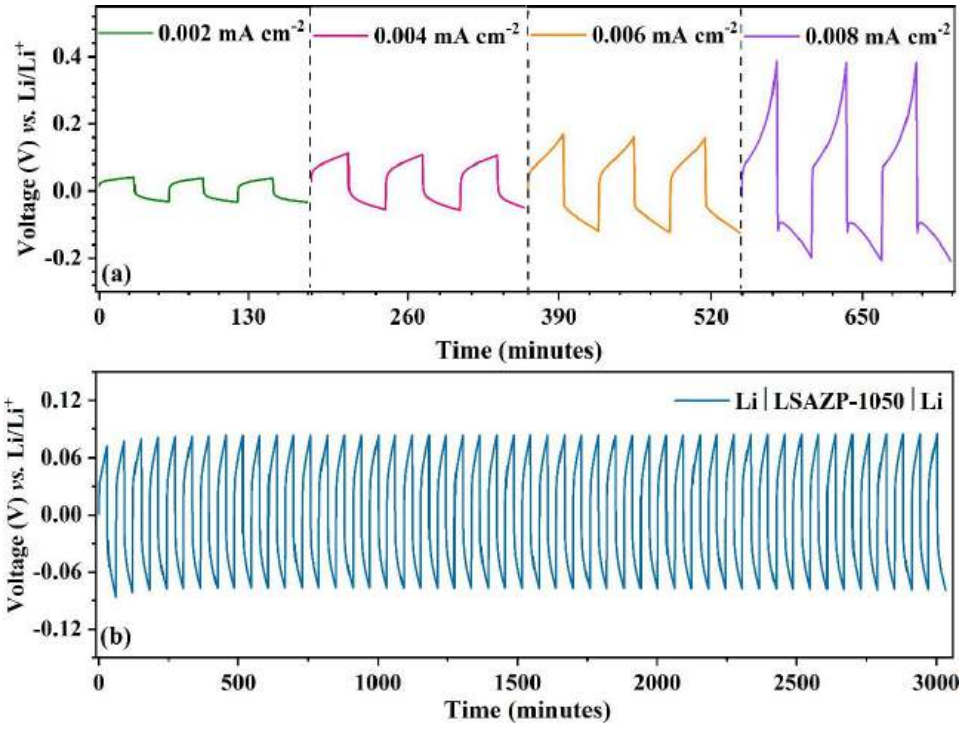

Fig. 8. (a) Voltage profile of Li|LSAZP-1050|Li cell at a different current density and (b) long-term lithium stripping-plating performance of Li|LSAZP-1050|Li cell at 4 μA *mA/cm^2 at RT.*

Incorporating inorganic and organic layers on the surface of ceramic-based electrolytes is often suggested as a potential solution to enhance the interfacial contact and stability between the electrolytes and lithium electrodes in literature [70-75]. This has lowered interfacial resistance and inhibited lithium dendrite growth by establishing homogeneous ion concentration gradients and suppressing local electric fields to ensure better Li^+ transport at the interface [70, 76, 77]. Further, the high room temperature Li^+ conductivity of LSAZP makes it an attractive, active filler candidate for composite electrolytes.

4. Conclusions

In summary, a medium entropy $Li_{1.5}Sn_{1.0}Al_{0.5}Zr_{0.5}(PO_4)_3$ solid electrolyte was fabricated *via* solid-state reaction method. The Rietveld refinement of XRD data confirmed a rhombohedral phase in the sample calcinated at 1050 °C. The temperature-dependent synchrotron XRD data confirmed a reversible anisotropic thermal expansion of the LSAZP unit cell. LSAZP sample sintered at 1050 °C exhibited an exceptional room temperature total conductivity of 2.95×10^{-4} S cm^{-1}. Significantly, no microcracks were observed in this sample, contributing to excellent room temperature conductivity. The Li-ion transference number was ~ 0.99, confirming that conduction in LSAZP is mostly ionic in nature. During galvanostatic lithium plating-stripping tests, the symmetric Li|LSAZP-1050|Li cell demonstrated stable lithium plating-stripping over 50 h at a current density of 4 μA cm^{-2} with only ~ 80 mV overpotential. These results are expected to open new avenues of research into NASICON-type electrolytes for their prospective application in all-solid-state lithium batteries.

Declaration of competing interest

The authors declare that they have no known competing financial interests or personal relationships that could have appeared to influence the work reported in this paper.

Acknowledgments

The authors thank the Science and Engineering Research Board (SERB) for the Core Research Grant (Grant no. CRG/2021/005548). Department of Science and Technology (DST), Government of India is also gratefully acknowledged for funding (Grant no. DST/TMD/IC-MAP/2K20/01).

Data availability

Data will be made available on request.

References

[1] M. Armand, J.M. Tarascon, Nature, 451 (2008) 652-657.

[2] A. Manthiram, X. Yu, S. Wang, Nat. Rev. Mater., 2 (2017).

[3] J.-M. Tarascon, Nat. Chem, 2 (2010) 510-510.

[4] T.-H. Kim, J.-S. Park, S.K. Chang, S. Choi, J.H. Ryu, H.-K. Song, Adv. Energy Mater., 2 (2012) 860-872.

[5] J.B. Goodenough, K.S. Park, JACS, 135 (2013) 1167-1176.

[6] B. Dunn, H. Kamath, J.M. Tarascon, Science, 334 (2011) 928-935.

[7] K. Xu, Chem. Rev., 114 (2014) 11503-11618.

[8] C. Yang, Q. Wu, W. Xie, X. Zhang, A. Brozena, J. Zheng, M.N. Garaga, B.H. Ko, Y. Mao, S. He, Y. Gao, P. Wang, M. Tyagi, F. Jiao, R. Briber, P. Albertus, C. Wang, S. Greenbaum, Y.-Y. Hu, A. Isogai, M. Winter, K. Xu, Y. Qi, L. Hu, Nature, 598 (2021) 590-596.

[9] A. Banerjee, X. Wang, C. Fang, E.A. Wu, Y.S. Meng, Chem. Rev., 120 (2020) 6878-6933.

[10] N. Kamaya, K. Homma, Y. Yamakawa, M. Hirayama, R. Kanno, M. Yonemura, T. Kamiyama, Y. Kato, S. Hama, K. Kawamoto, A. Mitsui, Nat. Mater, 10 (2011) 682-686.

[11] C. Yang, K. Fu, Y. Zhang, E. Hitz, L. Hu, Adv. Mater., 29 (2017) 1701169.

[12] Y.-S. Hu, Nat. Energy, 1 (2016) 16042.

[13] S. Shahid, M. Agelin-Chaab, Energy Convers. and Manag.: X, 16 (2022) 100310.

[14] A. Loutati, O. Guillon, F. Tietz, D. Fattakhova-Rohlfing, Open Ceram., 12 (2022) 100313.

[15] M.S. Whittingham, Chem. Rev., 104 (2004) 4271-4302.

[16] Z. Chen, G.-T. Kim, Z. Wang, D. Bresser, B. Qin, D. Geiger, U. Kaiser, X. Wang, Z. Shen, S. Passerini, Nano Energy, 64 (2019) 103986.

[17] S. Xin, Y. You, S. Wang, H.-C. Gao, Y.-X. Yin, Y.-G. Guo, ACS Energy Lett., 2 (2017) 1385-1394.

[18] K.B. Hatzell, X.C. Chen, C.L. Cobb, N.P. Dasgupta, M.B. Dixit, L.E. Marbella, M.T. McDowell, P.P. Mukherjee, A. Verma, V. Viswanathan, A.S. Westover, W.G. Zeier, ACS Energy Lett., 5 (2020) 922-934.

[19] B. Scrosati, Electrochim. Acta, 45 (2000) 2461-2466.

[20] M.R. Palacín, Chem. Soc. Rev., 38 (2009) 2565-2575.

[21] L. Yao, S. Xu, A. Tang, F. Zhou, J. Hou, Y. Xiao, Z. Fu, World electr. veh. j., 12 (2021) 113.

[22] J.B. Goodenough, Y. Kim, Chem. Mater., 22 (2010) 587-603.

[23] A. Manthiram, X. Yu, S. Wang, Nat. Rev. Mater., 2 (2017) 16103.

[24] K. Kang, Y.S. Meng, J. Bréger, C.P. Grey, G. Ceder, Science, 311 (2006) 977-980.

[25] Z. Jian, Y.-S. Hu, X. Ji, W. Chen, Adv. Mater., 29 (2017) 1601925.

[26] A.K. Das, M. Badole, H.N. Vasavan, S. Saxena, P. Gami, S. Kumar, Ceram. Int., 49 (2023) 29719-29728.

[27] F. Zheng, M. Kotobuki, S. Song, M. Lai, L. Lu, J. of Power Sources, 389 (2018) 198-213.

[28] B. Francisco, C. Stoldt, J.-C. M'Peko, Chem. Mater., 26 (2014) 4741-4749.

[29] M. Hou, F. Liang, K. Chen, Y. Dai, D. Xue, Nanotechnol., 31 (2020) 132003.

[30] Y. Zhang, K. Chen, Y. Shen, Y. Lin, C.W. Nan, Ceram. Int., 43 (2017).

[31] X. Pu, X. Cheng, Q. Yan, Y. Lin, R. Yan, R. Yang, X. Zhu, Ceram. Int., 50 (2024) 9007-9015.

[32] A.K. Das, M. Badole, H.N. Vasavan, S. Saxena, P. Gami, S. Deswal, P. Kumar, S. Kumar, MATER. TODAY SUSTAIN., 26 (2024) 100758.

[33] B. Tao, C. Ren, H. Li, B. Liu, X. Jia, X. Dong, S. Zhang, H. Chang, Adv. Funct. Mater., 32 (2022) 2203551.

[34] K. Singh, A. Chakraborty, R. Thirupathi, S. Omar, Ionics, 28 (2022) 5289-5319.

[35] I. Stenina, S. Novikova, D. Voropaeva, A. Yaroslavtsev, Batteries, 9 (2023).

[36] C. Sun, J. Liu, Y. Gong, D.P. Wilkinson, J. Zhang, Nano Energy, 33 (2017) 363-386.

[37] G.F. Ortiz, M.C. López, P. Lavela, C. Vidal-Abarca, J.L. Tirado, Solid State Ion., 262 (2014) 573-577.

[38] T. Pareek, S. Dwivedi, M. Badole, S. Kumar, Bull. Mater. Sci., 44 (2021) 177.

[39] S. Kumar, P. Balaya, Solid State Ion., 296 (2016) 1-6.

[40] H. Yamamoto, M. Tabuchi, T. Takeuchi, H. Kageyama, O. Nakamura, J. of Power Sources, 68 (1997) 397-401.

[41] Y. Li, M. Liu, K. Liu, C.-A. Wang, J. of Power Sources, 240 (2013) 50-53.

[42] I. Hanghofer, B. Gadermaier, A. Wilkening, D. Rettenwander, H.M.R. Wilkening, Dalton Trans., 48 (2019) 9376-9387.

[43] Q. Zhou, B. xu, P.-H. Chien, Y. Li, B. Huang, N. Wu, H. Xu, N. Grundish, Y.Y. Hu, J. Goodenough, Small Methods, 4 (2020) 2000764.

[44] V. Ramar, S. Kumar, S.R. Sivakkumar, P. Balaya, Electrochim. Acta, 271 (2018) 120-126.

[45] S. Ahmed, T. Pareek, S. Dwivedi, M. Badole, S. Kumar, J. Solid State Electrochem., 24 (2020).

[46] S.C. Kim, J. Wang, R. Xu, P. Zhang, Y. Chen, Z. Huang, Y. Yang, Z. Yu, S. Oyakhire, W. Zhang, L. Greenburg, M.S. Kim, D. Boyle, P. Sayavong, Y. Ye, J. Qin, Z. Bao, Y. Cui, Nat. Energy, 8 (2023) 1-13.

[47] A. Sarkar, Q. Wang, A. Schiele, M.R. Chellali, S.S. Bhattacharya, D. Wang, T. Brezesinski, H. Hahn, L. Velasco, B. Breitung, Adv. Mat., 31 (2019) 1806236.

[48] C. Oses, C. Toher, S. Curtarolo, Nat. Rev. Mater., 5 (2020) 295-309.

[49] M. Botros, J. Janek, Science, 378 (2022) 1273-1274.

[50] Y. Feng, L. Yang, Z. Yan, D. Zuo, Z. Zhu, L. Zeng, Y. Zhu, J. Wan, Energy Storage Mater., 63 (2023) 103053.

[51] L. Spiridigliozzi, G. Dell'Agli, S. Esposito, P. Rivolo, S. Grasso, V.M. Sglavo, M. Biesuz, Scr. Mater., 214 (2022) 114655.

[52] Y. Pu, S. Huang, P. Cao, 8 - High-entropy oxides for energy storage and catalysis, in: P. Cao, Z.-G. Chen, Z. Xia (Eds.) Advanced Ceramics for Energy Storage, Thermoelectrics and Photonics, Elsevier, 2023, pp. 209-236.

[53] A.A. Coelho, J. Appl. Crystallogr., 51 (2018) 210-218.

[54] A. Bondarenko, G. Ragoisha, Nova Science, (2005) 89-102.

[55] R.D. Shannon, C.T. Prewitt, Acta Crystallogr. B., 25 (1969) 925-946.

[56] H. Chen, L.L. Wong, S. Adams, Acta Crystallogr B Struct Sci Cryst Eng Mater, 75 (2019) 18-33.

[57] J. Ibañez, C. Pecharroman, R. Jimenez, P. Duran-Martin, M.G. Lazarraga, J.M. Rojo, J. Electrochem. Soc., 148 (2001) J31.

[58] D. Safanama, N. Sharma, R.P. Rao, H.E.A. Brand, S. Adams, J. Mater. Chem. A, 4 (2016) 7718-7726.

[59] M. Hou, T. Qu, Q. Zhang, Y. Yaochun, Y. Dai, F. Liang, G. Okuma, K. Hayashi, Corros. Sci., 177 (2020) 109012.

[60] S. Smith, T. Thompson, J. Sakamoto, J. Allen, D. Baker, J. Wolfenstine, Solid State Ion., 300 (2017) 38-45.

[61] J.T.S. Irvine, D.C. Sinclair, A.R. West, Adv. Mater., 2 (1990) 132-138.

[62] H. Xie, Y. Li, J.B. Goodenough, RSC Adv., 1 (2011) 1728-1731.

[63] C. Luo, M. Yi, Z. Cao, W. Hui, Y. Wang, ACS Appl. Elec. Mat., 6 (2024) 641-657.

[64] H. El Khal, A. Cordier, N. Batis, E. Siebert, S. Georges, M.C. Steil, Solid State Ion., 304 (2017) 75-84.

[65] D.J. Bergman, Ann. Phys. , 138 (1982) 78-114.

[66] D.J. Bergman, Phys. Rep., 43 (1978) 377-407.

[67] V. Thangadurai, W. Weppner, Chem. Mater., 14 (2002) 1136-1143.

[68] V. Thangadurai, W. Weppner, Adv. Funct. Mater., 15 (2005) 107-112.

[69] L. Jia, J. Zhu, X. Zhang, B. Guo, Y. Du, X. Zhuang, EER, 7 (2024) 12.

[70] Y. Hu, W. Li, J. Zhu, S.-M. Hao, X. Qin, L.-Z. Fan, L. Zhang, W. Zhou, Next Energy, 1 (2023) 100042.

[71] W. Zhou, S. Wang, Y. Li, S. Xin, A. Manthiram, J.B. Goodenough, JACS, 138 (2016) 9385-9388.

[72] Z. Zhang, S. Chen, J. Yang, G. Liu, X. Yao, P. Cui, X. Xu, Electrochim. Acta, 297 (2019) 281-287.

[73] X. Gao, X. Yang, M. Jiang, M. Zheng, Y. Zhao, R. Li, W. Ren, H. Huang, R. Sun, J. Wang, C.V. Singh, X. Sun, Adv. Funct. Mater., 33 (2023) 2209715.

[74] J. Zhang, C. Wang, M. Zheng, M. Ye, H. Zhai, J. Li, G. Tan, X. Tang, X. Sun, Nano Energy, 102 (2022) 107672.

[75] J. Zhang, J. Li, H. Zhai, G. Tan, X. Tang, ACS Appl. Energy Mater., 3 (2020) 6139-6145.

[76] C. Wang, W. Ping, Q. Bai, H. Cui, R. Hensleigh, R. Wang, A.H. Brozena, Z. Xu, J. Dai, Y. Pei, C. Zheng, G. Pastel, J. Gao, X. Wang, H. Wang, J.-C. Zhao, B. Yang, X. Zheng, J. Luo, Y. Mo, B. Dunn, L. Hu, Science, 368 (2020) 521-526.

[77] B. Li, Y. Chao, M. Li, Y. Xiao, R. Li, K. Yang, X. Cui, G. Xu, L. Li, C. Yang, Y. Yu, D. Wilkinson, J. Zhang, EER, 6 (2023) 7.

NASICON-type Medium Entropy $Li_{1.5}Sn_{1.0}Al_{0.5}Zr_{0.5}(PO_4)_3$ Electrolyte for Solid State Li Metal Batteries

[Supplementary Material]

Pratiksha Gami[a], Manish Badole[a], Hari Narayanan Vasavan[a], Asish Kumar Das[a], Samriddhi Saxena[a], Neha Dagar[a], Velaga Srihari[c], and Sunil Kumar[a,b]*

[a]Department of Metallurgical Engineering and Materials Science, Indian Institute of Technology Indore, Simrol, 453552, India.

[b]Center for Electric Vehicle and Intelligent Transport Systems, Indian Institute of Technology Indore, Simrol, 453552, India

[c]High Pressure & Synchrotron Radiation Physics Division, Bhabha Atomic Research Centre, 400085 Mumbai, India

* Corresponding author

Corresponding author E-mail: sunil@iiti.ac.in

.

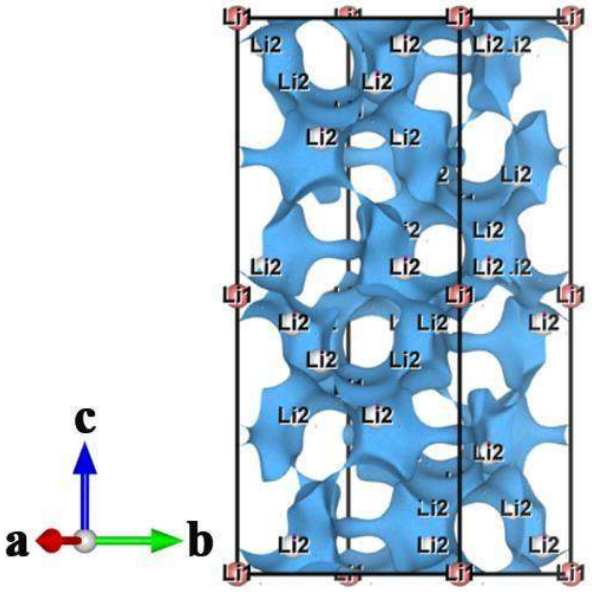

Fig. S1. Li-ion diffusion paths in the rhombohedral crystal structure of LSAZP-1050 are shown in three dimensions using blue isosurfaces that were produced using BVPA software.

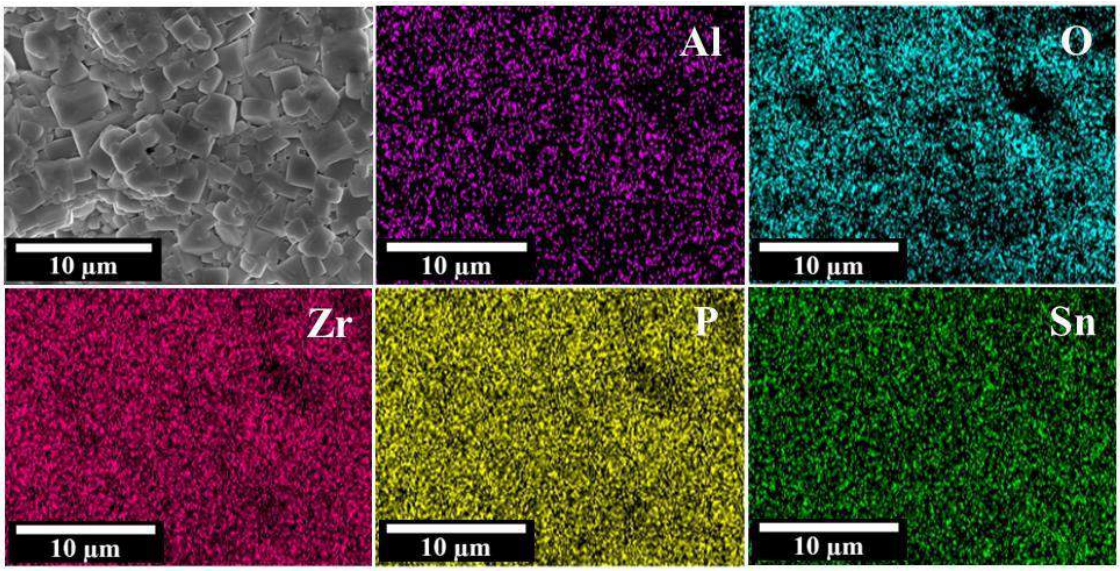

Fig. S2. SEM micrograph and EDS mappings of various elements of LSAZP-900 pellet.

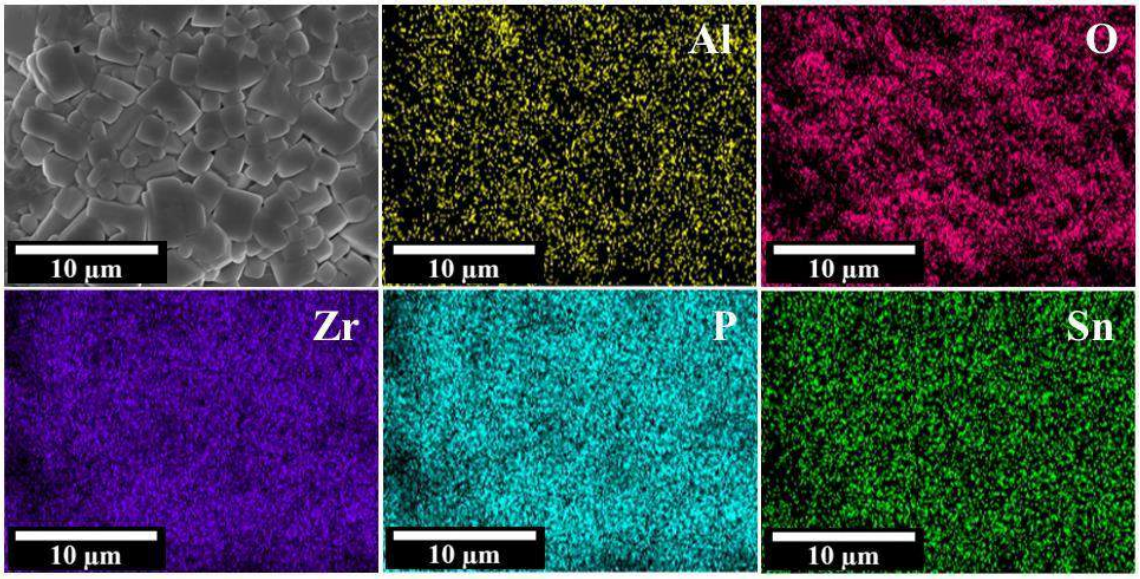

Fig. S3. SEM micrograph and EDS mappings of various elements of LSAZP-950 pellet.

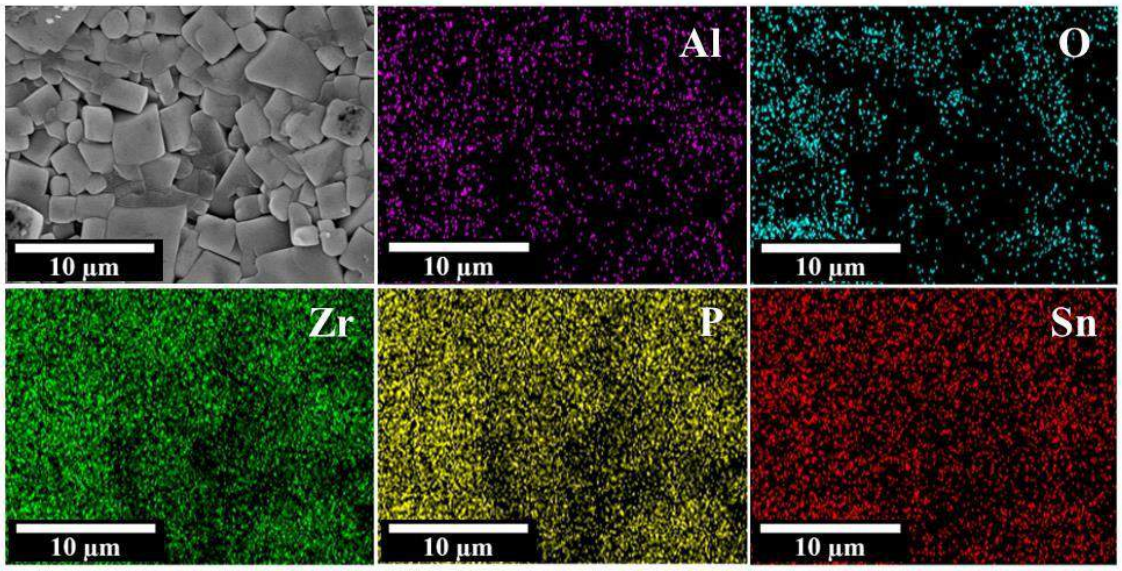

Fig. S4. SEM micrograph and EDS mappings of various elements of LSAZP-1000 pellet.

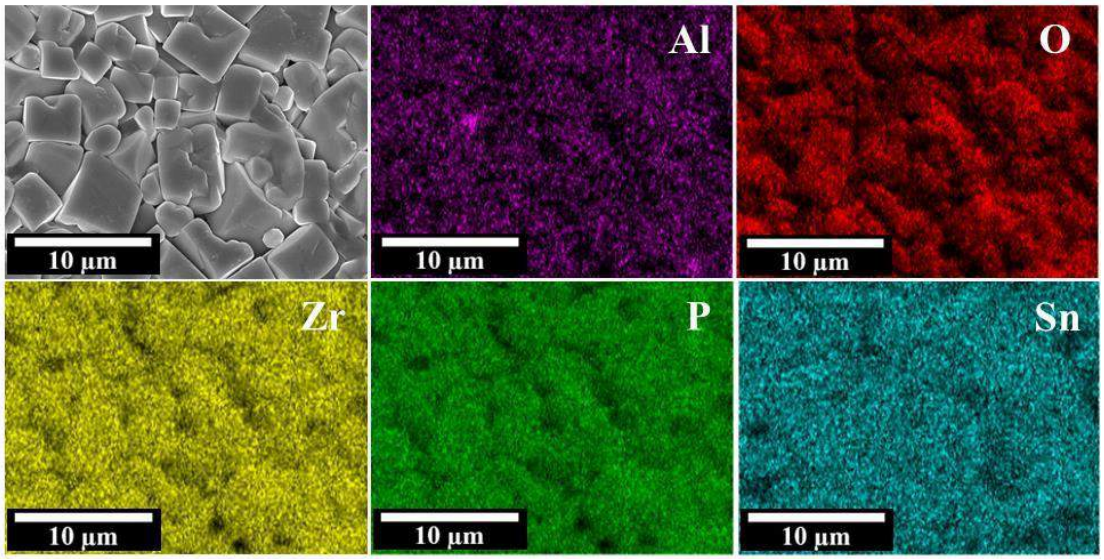

Fig. S5. SEM micrograph and EDS mappings of various elements of LSAZP-1100 pellet.

Table S1: Total conductivity of various NASICON-type materials sintered at different temperatures.

Inorganic Electrolyte	**Sintering Temperature (°C)**	**Total Conductivity ($S\ cm^{-1}$)**	**Reference**
$Li_{1.2}Al_{0.2}Zr_{1.8}(PO_4)_3$	1400	2.77×10^{-5}	[1]
$Li_{1.4}Sr_{0.2}Hf_{1.8}(PO_4)_3$	1100	1.62×10^{-5}	[2]
$Li_{1.2}Zr_{1.9}Ca_{0.1}(PO_4)_3$	1200	4.9×10^{-5}	[3]
$LiSnZr(PO_4)_3$	1000	1.45×10^{-5}	[4]
$LiTi_2(PO_4)_3$	1050	7.20×10^{-5}	[5]
$Li_{1.2}Y_{0.2}Zr_{1.8}(PO_4)_3$	1200	5.31×10^{-5}	[6]
$Li_{3.15}Sc_2Si_{0.15}P_{2.85}O_{12}$	1000	1.20×10^{-5}	[7]
$Li_{0.94}Zr_{1.94}Ta_{0.06}(PO_4)_3$	1200	6.06×10^{-5}	[8]

$Li_{1.5}Al_{0.3}Mg_{0.1}Ge_{1.6}(PO_4)_3$-$B_2O_3$	700	2.1×10^{-4}	[9]
$Li_{1.5}Al_{0.5}Ge_{1.5}(PO_4)_3$	850	3.1×10^{-4}	[10]
$Li_{1.3}Al_{0.3}Ti_{1.7}(PO_4)_3$	1000	7.0×10^{-4}	[11]
$Li_{1.5}Sn_{1.0}Al_{0.5}Zr_{0.5}(PO_4)_3$	1050	2.95×10^{-4}	**This work**

Table S2: Measured density, relative density, and activation energy of LSAZP pellets sintered at different temperatures.

Sintering Temperature (°C)	**Measured density (g/cm^3)**	**Relative density (%)**	**Activation energy (eV)**
900	2.72	79	0.76 ± 0.01
950	2.76	84	0.64 ± 0.03
1000	2.93	87	0.52 ± 0.002
1050	2.97	90	0.39 ± 0.02
1100	2.94	87	0.45 ± 0.01

Table S3: Electronic conductivity of LSAZP pellets sintered at different temperatures.

Sintering Temperature (°C)	**Electronic Conductivity (10^{-8}) (S cm^{-1})**
900	2.99
950	2.98

1000	3.03
1050	3.07
1100	3.04

References:

[1] B. Akkinepally, I.N. Reddy, T.J. Ko, K. Yoo, J. Shim, Ceram. Int., 48 (2022) 12142-12151.

[2] Q.-H. Li, C. Xu, B. Huang, X. Yin, Rare Met., 39 (2020) 1092-1098.

[3] H. Xie, Y. Li, J.B. Goodenough, RSC Advances, 1 (2011) 1728-1731.

[4] T. Pareek, S. Dwivedi, B. Singh, D. Kumar, P. Kumar, S. Kumar, J. Alloys Compd., 777 (2019) 602-611.

[5] V.R. Alaparthi, V. Veeraiah, A. Rao, B. Babu, B. Latha, R. Rao, Bull. Mater. Sci., 37 (2014) 883-888.

[6] P. Gami, M. Badole, H.N. Vasavan, A.K. Das, S. Saxena, S. Kumar, ACS Appl. Eng. Mater., 2 (2024) 1278-1287.

[7] A. Loutati, O. Guillon, F. Tietz, D. Fattakhova-Rohlfing, Open Ceram., 12 (2022) 100313.

[8] X. Pu, X. Cheng, Q. Yan, Y. Lin, R. Yan, R. Yang, X. Zhu, Ceram. Int., 50 (2024) 9007-9015.

[9] S. Saffirio, H. Darjazi, M.E. Coller Pascuzzi, F. Smeacetto, C. Gerbaldi, Heliyon, 10 (2024) e24493.

[10] Y. Liu, J. Chen, J. Gao, Solid State Ion., 318 (2018) 27-34.

[11] H. Aono, E. Sugimoto, Y. Sadaoka, N. Imanaka, G.y. Adachi, J. Electrochem. Soc., 137 (1990) 1023.